PDE-free method for the numerical bifurcation and stability analysis of fluid flows via machine learning

Alessandro Della Pia[1], Dimitrios G. Patsatzis[2], Gianluigi Rozza[1], Lucia Russo[3,*], Constantinos Siettos[4,*]
Corresponding authors: lucia.russo@stems.cnr.it, constantinos.siettos@unina.it
[1] SISSA, International School for Advanced Studies, Mathematics Area, mathLab, Trieste, 34136, Italy.
[2] Modelling and Engineering Risk and Complexity, Scuola Superiore Meridionale, School for Advanced Studies, Naples, 80128, Italy.
[3] Institute of Science and Technology for Energy and Sustainable Mobility (STEMS), Consiglio Nazionale delle Ricerche (CNR), Naples, 80125, Italy.
[4] Dipartimento di Matematica e Applicazioni "Renato Caccioppoli", Università degli Studi di Napoli "Federico II", Naples, 80126, Italy.

Abstract: Numerical bifurcation and stability analysis of high-fidelity Navier–Stokes simulations is severely limited by the cost of assembling and factorizing the large Jacobians required by continuation software such as AUTO and MATCONT, rendering tasks like limit-cycle continuation intractable beyond small-scale test cases. We present a PDE-free, fully data-driven "restrict–learn–lift" pipeline that circumvents this bottleneck. High-dimensional spatio-temporal snapshots generated by direct numerical simulation of the incompressible Navier–Stokes equations are first projected onto a minimal-dimensional latent space via Proper Orthogonal Decomposition (POD); a surrogate reduced-order model (ROM) of the latent dynamics is then learned with Gaussian Process regression (GPR); numerical continuation and stability analysis (fixed points, limit cycles, Floquet multipliers) are subsequently carried out directly on the learned ROM using the MATCONT toolbox; finally, the bifurcating states are reconstructed in the physical space through the closed-form POD pre-image mapping. We demonstrate the approach on the two-dimensional wake flow past a circular cylinder, for which POD naturally identifies the correct two-dimensional latent space and the pipeline accurately reconstructs the Andronov–Hopf bifurcation at $Re_{cr} \approx 49$, including the continuation of the emerging limit-cycle branch, its period, and its Floquet multipliers. While POD is sufficient to resolve this primary instability, we discuss why more demanding, secondary bifurcation scenarios—such as symmetry-breaking and Neimark–Sacker bifurcations—require nonlinear manifold-learning techniques, such as Diffusion Maps, to correctly identify the intrinsic dimensionality of the latent dynamics; this extension is thoroughly explored in a companion study [1].

Keywords: Fluid Dynamics, Navier-Stokes PDEs, Reduced-Order Models, Proper Orthogonal Decomposition, Numerical Bifurcation Analysis, Machine Learning, Gaussian Process Regression.

1. Introduction

Numerical simulations of nonlinear phenomena in fluid mechanics have reached an unprecedented level of detail thanks to the continued advancement of computational algorithms and hardware resources. Yet understanding the mechanisms that govern complex phenomena, such as flow instabilities and the onset of turbulence, requires more than time-marching simulations: while modern Computational Fluid Dynamics (CFD) codes efficiently integrate transients and even locate steady states via Newton solvers, they cannot reliably pinpoint the critical (tipping) points at which instabilities appear, nor trace the resulting unstable branches. A systematic and precise analysis of the emergence and evolution of oscillatory patterns—even unstable ones that can explain the route to turbulence—requires a systematic bifurcation analysis. The numerical bifurcation theory toolkit offers a suite of algorithms and software tools, such as AUTO [2] and MATCONT [3, 4], that facilitate the continuation of stable and unstable steady states, limit cycles, and critical bifurcation points, including Hopf, fold, period-doubling and Neimark–Sacker bifurcations, as well as codimension-2 bifurcation tracking. However, for high-fidelity CFD simulations, storing and factorizing the high-dimensional Jacobian matrices required by these packages renders tasks such as limit-cycle continuation computationally intractable beyond small-scale test cases [5]. Matrix-free Krylov subspace methods, such as Newton–Krylov solvers, offer a scalable alternative for large-scale PDE systems by avoiding the explicit formation of Jacobians [5, 6, 7, 8, 9, 10, 11]; for the Navier–Stokes equations, Newton–Krylov continuation of periodic orbits has been performed in [6]. Nonetheless, such methods lack the comprehensive algorithmic capabilities—robust detection and continuation of codimension-1 and codimension-2 bifurcations, user-friendly interfaces—of the established continuation packages, and typically require custom implementation for each new problem.

Reduced-order models (ROMs) in CFD [12, 13, 14, 15, 16, 17, 18, 19] reduce the computational and memory cost by orders of magnitude, enabling both faster simulations and the systematic bifurcation analysis that would be prohibitive for the full-order model. The rationale is that, despite their inherently nonlinear behaviour, fluid flows often organize around a few dominant coherent structures that carry the essential information about the emergent dynamics across the parameter space—the derivation of the Lorenz equations from a low-dimensional truncation of Rayleigh–Bénard convection being a paradigmatic example. A prominent class of such ROMs is represented by *normal-forms*, i.e., the simplest possible reduced models of a high-dimensional dynamical system around a bifurcation point [20], obtained by systematically truncating nonessential dimensions and higher-order terms. Traditionally, such ROMs are derived by linearizing the full Navier–Stokes equations around a base state and identifying the critical eigenmodes with near-zero growth rate, then using invariant/center manifold theory [13, 21, 22, 23, 24, 25] or spectral submanifold theory [26, 27, 28] to parameterize a locally invariant, low-dimensional manifold tangent to those modes. The theory of approximate inertial manifolds [13, 14, 29, 30, 31] has similarly been used to construct finite-dimensional manifolds onto which Navier–Stokes trajectories are exponentially attracted.

Data-driven methods have recently complemented this analytical machinery by learning surrogate ROMs directly from high-fidelity spatio-temporal simulations [18, 32, 33, 34]. The typical pipeline first projects the flow onto a low-dimensional latent space via manifold learning, most commonly Proper Orthogonal Decomposition (POD) [35, 36, 37, 38], which offers a direct, closed-form solution to the pre-image (reconstruction) problem. Nonlinear manifold-learning algorithms, such as Diffusion Maps (DMs) [39, 40, 41, 42, 43, 44, 45], have also been exploited to deal with more complex dynamics, at the cost of an inherently ill-posed pre-image problem. On the modelling side, several approaches have been used to learn the evolution operator on the latent space, including sparse identification of nonlinear dynamics (SINDy) [46, 47, 48], feed-forward and recurrent neural networks [43, 49, 50], and Gaussian Process regression (GPR) [51, 52, 53, 54], which also provides a natural quantification of predictive uncertainty. In [19, 55, 56], ROMs and bifurcation diagrams of equilibria are built from steady-state snapshots via intrusive POD-Galerkin projections; this approach has also been used for the control of solutions on unstable branches [57] and extended to fluid–structure interaction [58]. In [48], POD and autoencoders are combined with parametric SINDy to enable efficient bifurcation analysis, with applications including the flow past a cylinder.

Building on the celebrated Equation-Free (EF) multiscale framework [59, 60], which is rooted in the on-demand construction of local models from short bursts of a microscopic (or high-fidelity) simulator, we propose here a PDE-free, fully data-driven "restrict–learn–lift" framework for constructing surrogate normal-forms that approximate, both qualitatively and quantitatively, the emergent dynamics of the Navier–Stokes equations, enabling their use in state-of-the-art numerical bifurcation and stability analysis toolkits such as MATCONT [3, 61] and AUTO [2]—tasks that would otherwise be computationally intractable in the high-dimensional state space of the full-order simulator, where one typically must resort to linear (or weakly nonlinear) stability analysis of equilibria and local theoretical normal forms [62]. A closely related EF strategy, coupled with POD, was previously used for incompressible flows in [63]; the key distinction of the present approach is that, rather than constructing local mappings on-the-fly from short bursts of microscopic simulation, a single global surrogate model is learned from long-term, high-fidelity simulations spanning the entire parameter range, which can subsequently be probed with the full arsenal of continuation algorithms.

In this paper, we focus the presentation and validation of the framework on a single, well-understood benchmark: the two-dimensional wake flow past a circular cylinder, which undergoes a supercritical Andronov–Hopf bifurcation as the Reynolds number *Re* is increased [64, 65]. We show that a minimal, two-dimensional POD-based latent space, coupled with a GPR surrogate and MATCONT continuation, reproduces with high accuracy the full bifurcation diagram—the loss of stability of the steady wake, the emerging limit-cycle branch, its period, and its Floquet multipliers—and that these results can be reconstructed back into the original high-dimensional velocity field via the closed-form POD pre-image mapping. Because the cylinder wake instability is a *primary* bifurcation, POD suffices to identify the correct minimal dimension of the reduced dynamics. This is, however, not the case for *secondary* bifurcations that arise on top of an already-established limit cycle (e.g. a Neimark–Sacker bifurcation leading to quasi-periodic, torus-like dynamics) or for symmetry-breaking pitchfork bifurcations, where the latent geometry becomes strongly curved and POD may fail to identify the correct intrinsic dimensionality, or require spurious extra modes that do not correspond to the true normal-form dimension. In a companion study [1], we show that nonlinear manifold learning via parsimonious Diffusion Maps [42, 45] is required in such cases, and demonstrate the resulting DMs-based ROMs on the sudden-expansion (Coanda) channel flow, which exhibits a symmetry-breaking pitchfork bifurcation, and on the fluidic pinball, which exhibits a secondary Neimark–Sacker bifurcation and the associated birth of an invariant torus.

The rest of the paper is organized as follows. Section 2 describes the four-stage PDE-free methodology: the governing equations, the POD-based restriction/embedding, the GPR-based learning of the latent dynamics, the numerical bifurcation and stability analysis toolkit, and the closed-form lifting back to the physical space. Section 3 describes the cylinder wake flow configuration and the direct numerical simulation setup. Results are presented in Section 4, followed by a discussion, in Section 5, of why more complex bifurcation scenarios call for nonlinear manifold learning. Conclusions are provided in Section 6.

2. Methodology

The proposed pipeline—rooted in the Equation-Free (EF) multiscale numerical analysis framework [59]—for the systematic, PDE-free bifurcation and stability analysis of the Navier–Stokes equations consists of four main steps: (a) use manifold learning (here, Proper Orthogonal Decomposition) to "restrict/embed" the high-dimensional spatio-temporal flow field into a low-dimensional latent space; (b) learn a surrogate ROM of the latent dynamics (here, via Gaussian Process regression, which additionally allows for uncertainty quantification); (c) perform numerical bifurcation and stability analysis directly in the latent space (here, via MATCONT); (d) "lift" the resulting bifurcation diagram back to the high-dimensional physical space. A key distinction between this framework and the traditional EF approach coupled with POD for incompressible flows [63] is that, in the latter, one constructs local mappings and computes the quantities needed for bifurcation analysis via short, on-demand bursts of microscopic simulation. In contrast, the present method learns a single global surrogate model via machine learning from long-term, high-fidelity simulations spanning the entire parameter range, which can then be queried by the full continuation toolkit without any further recourse to the Navier–Stokes solver—hence *PDE-free*.

2.1 Governing equations

For our illustration, we consider the incompressible two-dimensional Navier–Stokes partial differential equations in dimensionless form:

$$\frac{\partial u}{\partial x}+\frac{\partial v}{\partial y} = 0, \tag{1a}$$

$$\frac{\partial u}{\partial t}+u\frac{\partial u}{\partial x}+v\frac{\partial u}{\partial y} = -\frac{\partial p}{\partial x}+\frac{1}{Re}\left(\frac{\partial^2 u}{\partial x^2}+\frac{\partial^2 u}{\partial y^2}\right), \tag{1b}$$

$$\frac{\partial v}{\partial t}+u\frac{\partial v}{\partial x}+v\frac{\partial v}{\partial y} = -\frac{\partial p}{\partial y}+\frac{1}{Re}\left(\frac{\partial^2 v}{\partial x^2}+\frac{\partial^2 v}{\partial y^2}\right), \tag{1c}$$

where $u \equiv u(x, y, t)$ and $v \equiv v(x, y, t)$ are the streamwise and normal-to-flow velocity components across the two-dimensional spatial domain (x, y) over time t, and $p \equiv p(x, y, t)$ denotes the pressure. The bifurcation parameter is the Reynolds number Re, defined in Eq. (20) of Section 3 for the cylinder wake configuration considered here.

2.2 Restriction to a POD-based latent space

Let $\{\mathbf{u}_m\}_{m=1,\dots,M}$ denote a given set of spatio-temporal snapshots arising from the discretized Navier–Stokes equations. Each snapshot at time t_m stacks the velocity components on the whole spatial grid, $\mathbf{u}_m = [u(x_i, y_j, t_m), v(x_i, y_j, t_m)]^\top \in \mathbb{R}^N$, where $i = 1, \dots, N_x$, $j = 1, \dots, N_y$, and $N = 2N_g$, with $N_g = N_x \times N_y$ the total number of grid points. We assume that these points lie on a smooth d-dimensional manifold $\mathcal{M} \subset \mathbb{R}^N$, and seek a data-driven restriction map

$$\Phi : \mathbb{R}^N \longrightarrow A \subset \mathbb{R}^d, \quad d \ll N, \tag{2}$$

such that $\mathbf{a}_m = \Phi(\mathbf{u}_m) \in \mathbb{R}^d$ captures the dominant coherent structures and emergent dynamics of the flow, with d an approximation of the intrinsic dimension of $\mathcal{M}$.

For each value of the governing parameter Re, we evaluate the fluctuations of the velocity field $\mathbf{u}(x, y, t) = [u(x, y, t), v(x, y, t)]^\top$ about the temporal mean $\overline{\mathbf{u}}(x, y)$, namely $\mathbf{u}'(x, y, t) = \mathbf{u}(x, y, t) - \overline{\mathbf{u}}(x, y)$. The classical POD technique [66] decomposes these fluctuations as

$$\mathbf{u}'(x, y, t) = \sum_{i=1}^{\infty} a_i(t)\boldsymbol{\varphi}_i(x, y), \tag{3}$$

where the modes $\boldsymbol{\varphi}_i(x, y)$ are spatially orthogonal. Defining $\mathbf{S}' = \{\mathbf{u}'_m\}_{m=1,\dots,M} \in \mathbb{R}^{N\times M}$, the discrete POD modes are obtained via the method of snapshots [67], leading to the eigenvalue problem for the snapshot covariance matrix $\mathbf{S}'^\top\mathbf{S}' \in \mathbb{R}^{M\times M}$:

$$\mathbf{S}'^\top\mathbf{S}'\boldsymbol{\psi}_i = \lambda_i\boldsymbol{\psi}_i, \quad i = 1, \dots, M, \tag{4}$$

where $\boldsymbol{\varphi}_i = \mathbf{S}'\boldsymbol{\psi}_i/\sqrt{\lambda_i}$ and $\lambda_i \geq 0$ are sorted in descending order, $\lambda_1 \geq \dots \geq \lambda_M$. Retaining the leading $d \ll M < N$ modes yields a reduced-order POD basis providing a linear parametrization of the manifold $\mathcal{M}$. Using this basis, the restriction map Φ of Eq. (2) reads

$$\mathbf{a} = \Phi(\mathbf{u}) = \mathbf{W}^\top(\mathbf{u} - \overline{\mathbf{u}}), \tag{5}$$

where $\mathbf{W} = [\boldsymbol{\varphi}_1, \dots, \boldsymbol{\varphi}_d] \in \mathbb{R}^{N\times d}$ and $\mathbf{a} = [a_1, \dots, a_d]^\top$ are the leading POD coefficients. Crucially for the closing (lifting) stage of the pipeline, the POD basis provides a *closed-form* solution to the pre-image problem: for any latent point $\mathbf{a}_*$, the corresponding high-dimensional field is reconstructed exactly as

$$\hat{\mathbf{u}}_* = \Psi(\mathbf{a}_*) = \overline{\mathbf{u}} + \mathbf{W}\mathbf{a}_*. \tag{6}$$

This is in marked contrast with nonlinear manifold-learning techniques, such as Diffusion Maps, for which the pre-image problem is inherently ill-posed and must be solved approximately, e.g., via geometric harmonics, kernel ridge regression, or the k-nearest-neighbour algorithm [68, 69, 44]. We discuss in Section 5 why such nonlinear embeddings become necessary once the flow undergoes more complex, secondary bifurcations.

2.3 Numerical solution of the Navier–Stokes equations for data acquisition

To acquire the high-dimensional flow data on which the ROM is constructed, we solve the incompressible Navier–Stokes equations (1a)–(1c), with appropriate boundary and initial conditions detailed in Section 3, by means of the open-source code BASILISK (`http://basilisk.fr`), which implements a second-order accurate finite-volume scheme. As is standard for incompressible flows, the equations are solved via the projection method on a uniform structured grid of $N_g = N_x \times N_y$ points: a temporary velocity field is first computed by ignoring the pressure gradient, and is then projected onto the space of divergence-free velocity fields by adding the appropriate pressure-gradient correction. Full details of the numerical schemes implemented in BASILISK can be found in [70].

To construct the restriction map Φ across the pre- and post-bifurcation regimes, we perform N_{Re} direct numerical simulations with Re uniformly distributed in $[Re_{min}, Re_{max}]$. For each value of Re, we record N_t snapshots of the velocity field, collected in the snapshot matrix $\mathbf{S} = \{\mathbf{u}_m\}_{m=1,\dots,M} \in \mathbb{R}^{N\times M}$, with $N = 2N_g$ and $M = N_t \times N_{Re}$.

2.4 ROMs via Gaussian Process regression

Having obtained the latent coordinates $\mathbf{a}(t) = \Phi(\mathbf{u}(t)) \in \mathbb{R}^d$ via the POD restriction map, we learn the unknown evolution operator governing the embedded dynamics via Gaussian Process regression (GPR). We model the dynamics in continuous time,

$$\frac{d\mathbf{a}(t)}{dt} \;=\; \boldsymbol{g}\big(\mathbf{a}(t), Re\big) \;+\; \mathbf{e}(t), \tag{7}$$

where $\mathbf{e}(t)$ represents unmodelled noise, and the regression map $\boldsymbol{g}$ is learned by solving

$$\min_{\mathbf{g}\in G,\, \boldsymbol{\theta}\in\mathbb{R}^l} \mathcal{L}\Big(\frac{d\mathbf{a}_m}{dt}, \mathbf{g}\big(\mathbf{a}_m, Re_m; \boldsymbol{\theta}\big)\Big), \quad \frac{d\widehat{\mathbf{a}}_m}{dt} = \mathbf{g}\big(\mathbf{a}_m, Re_m; \boldsymbol{\theta}\big), \tag{8}$$

over the M observations, where $\mathcal{L}$ quantifies the prediction error of the time-derivative estimation (here, mean-squared error).

The GPR surrogate model for each component a_i, $i = 1, \dots, d$, of the latent state, takes the form

$$\frac{da_i}{dt} \;=\; g_i\big(\mathbf{a}, Re; \boldsymbol{\theta}_i\big) \;+\; e_i, \qquad e_i \sim \mathcal{N}(0, \sigma_i^2), \tag{9}$$

where, dropping the time dependence for conciseness, each $g_i(z; \boldsymbol{\theta}_i) = g_i([\mathbf{a}, Re]^\top; \boldsymbol{\theta}_i)$ is an independent Gaussian Process $g_i \sim \mathcal{GP}(0, k_i(\mathbf{z}, \mathbf{z}'|\boldsymbol{\theta}_i))$ with zero mean and kernel $k_i(\cdot)$. Collecting the M observations $z_m = [\mathbf{a}_m, Re_m]^\top$ in $\boldsymbol{Z} = [z_1, \dots, z_M]^\top \in \mathbb{R}^{M\times(d+1)}$, predictions at a new point $z_* \in \mathbb{R}^{d+1}$ follow the posterior conditional distribution $g_i(z_*) \sim \mathcal{N}(\mu_{i,*}, \sigma_{i,*}^2)$, with

$$\mu_{i,*} = \boldsymbol{k}_i(z_*, \boldsymbol{Z} \mid \boldsymbol{\theta}_i) \left[\boldsymbol{K}_i(\boldsymbol{Z}, \boldsymbol{Z} \mid \boldsymbol{\theta}_i) + \sigma_i^2 \boldsymbol{I}_M\right]^{-1} \tfrac{d\mathbf{a}_i}{dt}, \tag{10}$$

$$\sigma_{i,*}^2 = k_i(z_*, z_* \mid \boldsymbol{\theta}_i) - \boldsymbol{k}_i(z_*, \boldsymbol{Z} \mid \boldsymbol{\theta}_i) \left[\boldsymbol{K}_i(\boldsymbol{Z}, \boldsymbol{Z} \mid \boldsymbol{\theta}_i) + \sigma_i^2 \boldsymbol{I}_M\right]^{-1} \boldsymbol{k}_i(\boldsymbol{Z}, z_* \mid \boldsymbol{\theta}_i), \tag{11}$$

where $\boldsymbol{K}_i(\boldsymbol{Z}, \boldsymbol{Z}) \in \mathbb{R}^{M\times M}$ is the covariance matrix with entries $k_i(z_m, z_l \mid \boldsymbol{\theta}_i)$. The hyperparameters $\boldsymbol{\theta}_i$

and noise variance σ_i^2 are estimated by minimizing the negative log marginal likelihood

$$-\log P\left(\tfrac{d\mathbf{a}_i}{dt} \mid \boldsymbol{Z}, \boldsymbol{\theta}_i\right) = \frac{1}{2}\left(\tfrac{d\mathbf{a}_i}{dt}\right)^\top \boldsymbol{\Sigma}_i^{-1}\tfrac{d\mathbf{a}_i}{dt} + \frac{1}{2}\log|\boldsymbol{\Sigma}_i| + \frac{M}{2}\log 2\pi, \tag{12}$$

with $\boldsymbol{\Sigma}_i = \boldsymbol{K}_i(\boldsymbol{Z}, \boldsymbol{Z} \mid \boldsymbol{\theta}_i) + \sigma_i^2 \boldsymbol{I}_M$. We employ a radial basis function kernel with automatic relevance determination (ARD):

$$k_i(z_m, z_l \mid \boldsymbol{\theta}_i) = (\theta_{i,1})^2 \exp\left(-\sum_{j=1}^{d+1} \frac{(z_{m,j} - z_{l,j})^2}{2(\theta_{i,j+1})^2}\right), \tag{13}$$

where $z_{m,j} = a_{m,j}$ for $j = 1, \ldots, d$ and $z_{m,d+1} = Re_m$. Finally, given the POD embeddings $\mathbf{a}_m$ and the corresponding Re_m values, we estimate the time derivatives $da_{m,i}/dt$ by finite differences and determine $\boldsymbol{\theta}_i$ by minimizing Eq. (12), yielding the resulting GPR model for the latent dynamics

$$\begin{cases} \dfrac{da_1}{dt} = g_1(a_1, \ldots, a_d, Re), \\ \quad\vdots \\ \dfrac{da_d}{dt} = g_d(a_1, \ldots, a_d, Re). \end{cases} \tag{14}$$

2.5 Numerical bifurcation analysis

The identified latent-space model (14) enables tracking stationary states and assessing their stability, allowing the construction of coarse-grained bifurcation diagrams. Stable stationary states are obtained by numerically finding the roots $\mathbf{a}_*$ of

$$\mathbf{g}(\mathbf{a}, Re) = \mathbf{0}, \tag{15}$$

via a Newton–Raphson scheme, where $\mathbf{g} = [g_1, \ldots, g_d]$ is the learned latent dynamics operator. Unstable stationary states are tracked via pseudo arc-length continuation, augmenting Eq. (15) with the condition

$$N(\mathbf{a}, Re) = \mathbf{c}\cdot(\mathbf{a} - \mathbf{a}_1) + b(Re - Re_1) = 0, \qquad \mathbf{c} \equiv \frac{(\mathbf{a}_1 - \mathbf{a}_0)^\top}{\delta s}, \qquad b \equiv \frac{Re_1 - Re_0}{\delta s}, \tag{16}$$

where $(\mathbf{a}_0, Re_0)$ and $(\mathbf{a}_1, Re_1)$ are two previously computed points along the branch and δs is the pseudo arc-length step. In practice, the next stationary state is obtained by solving the linearized $(d + 1)$-dimensional system

$$\begin{bmatrix} \dfrac{\partial \mathbf{g}}{\partial \mathbf{a}} & \dfrac{\partial \mathbf{g}}{\partial Re} \\ \mathbf{c} & b \end{bmatrix} \begin{bmatrix} \delta\mathbf{a} \\ \delta Re \end{bmatrix} = -\begin{bmatrix} \mathbf{g}(\mathbf{a}, Re) \\ N(\mathbf{a}, Re) \end{bmatrix}, \tag{17}$$

via the Moore–Penrose pseudo-inverse, until a predefined tolerance is reached. Once a stationary state $(\mathbf{a}_*, Re_*)$ is obtained, its stability follows from the eigenvalues σ_i of the Jacobian $\partial\mathbf{g}/\partial\mathbf{a}$: the state is stable if $\mathrm{Re}(\sigma_i) < 0$ for all i, unstable if $\mathrm{Re}(\sigma_i) > 0$ for some i, with a bifurcation occurring when $\mathrm{Re}(\sigma_i) = 0$. Codimension-1 bifurcations (Hopf, fold, branching points) mark critical transitions, with Hopf bifurcations giving rise to limit cycles; codimension-2 bifurcations and detailed criteria can be found in [71].

If a branch of limit cycles emerges, one seeks periodic solutions $\mathbf{a}(t) = \mathbf{a}(t + T)$, $\forall t$, where the period T is treated as an unknown parameter. Rescaling time as $\tau = t/T$, the boundary value problem reads

$$\begin{cases} \dfrac{d\mathbf{a}}{d\tau} - T\mathbf{g}(\mathbf{a}, Re) = 0, \\ \quad \mathbf{a}(0) - \mathbf{a}(1) = 0, \end{cases} \tag{18}$$

(a)

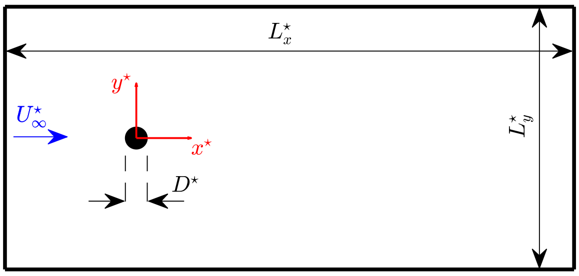

Figure 1: Schematic representation of the wake flow past a circular cylinder.

augmented with a phase condition removing translational invariance,

$$\int_0^1 \langle \mathbf{a}(\tau), \dot{\mathbf{a}}_0(\tau) \rangle d\tau = 0, \tag{19}$$

where $\dot{\mathbf{a}}_0$ is the derivative of a previously computed limit cycle. Continuation of limit cycles proceeds analogously to Eq. (17), discretizing $\mathbf{a}$ over collocation points; stability is assessed via Floquet multipliers, which also reveal secondary bifurcation points such as period-doubling, fold, branching, or Neimark–Sacker bifurcations [71].

For the implementation of numerical bifurcation analysis, we employed MATCONT [3, 4], which provides tools for continuation and identification of bifurcation points for stationary states and limit cycles. The learned GPR ROM of Eq. (14) is supplied to MATCONT, and derivatives required in Eq. (17) are computed numerically. MATCONT employs direct numerical solvers for Eq. (17), which would be intractable for the full Navier–Stokes equations, especially for limit cycles; matrix-free Krylov methods [5, 9, 10, 11] can handle large systems but lack the full bifurcation-analysis capabilities of MATCONT. Our framework performs all continuation and bifurcation analysis in the low-dimensional latent space, and reconstructs solutions in the high-dimensional physical space via the closed-form lifting map Ψ of Eq. (6).

3. Flow configuration: wake flow past a circular cylinder

The two-dimensional flow around an infinitely long circular cylinder immersed in a uniform stream is considered. A Cartesian coordinate system $Ox^\star y^\star$ is placed at the cylinder centre, with the $x^\star$ axis aligned with the flow direction and the $y^\star$-axis normal to it. The cylinder diameter is $D^\star$ and the free-stream velocity is $U_\infty^\star$. The Reynolds number is defined as

$$Re = \frac{\rho U_\infty^\star D^\star}{\mu}, \tag{20}$$

where ρ and μ are the fluid density and dynamic viscosity, respectively (dimensional quantities, except fluid properties, are denoted with the superscript $\star$).

Direct numerical simulations of the incompressible Navier–Stokes equations (see Section 2.3) are used to compute the two-dimensional viscous wake behind the cylinder. All physical quantities are made dimensionless with respect to $D^\star$ and $U_\infty^\star$:

$$x = \frac{x^\star}{D^\star}, \quad y = \frac{y^\star}{D^\star}, \quad u = \frac{u^\star}{U_\infty^\star}, \quad v = \frac{v^\star}{U_\infty^\star}, \quad p = \frac{p^\star}{\rho U_\infty^{\star 2}}, \quad t = t^\star \frac{U_\infty^\star}{D^\star}. \tag{21}$$

The computational domain is a rectangle excluding the interior of the cylinder, with sides $L_x^\star = 26D^\star$ and $L_y^\star = 12D^\star$ (Fig. 1). A no-slip boundary condition is applied on the fixed cylinder surface. At the domain inlet, a uniform velocity profile $u = 1$, $v = 0$ is prescribed, which also serves as the initial condition.

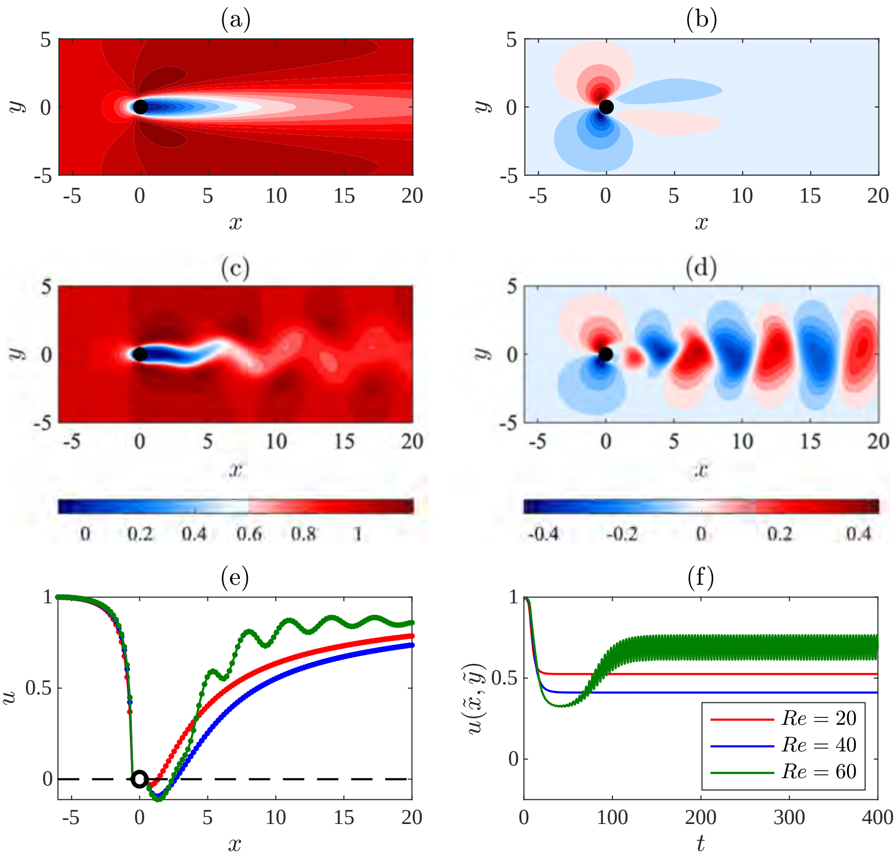

Figure 2: Instantaneous contour maps of u ((a) and (c)) and v ((b) and (d)) velocity components of the cylinder flow for $Re = 20$ ((a)-(b)) and $Re = 60$ ((c)-(d)). Panel (e) reports the instantaneous spatial distribution of u on the $y = 0$ axis for $Re = 20$, 40 and 60. Panel (f) shows the temporal evolution of u at $(\tilde{x}, \tilde{y}) = (7, 0)$ for the same values of Re.

A standard free-outflow boundary condition is enforced on the outlet, while the remaining sides are equipped with homogeneous Neumann boundary conditions. A uniform structured grid with mesh size $\Delta x = \Delta y = 0.2$ is used (five grid cells per cylinder diameter), yielding $N_g = N_x \times N_y = 7800$ grid points—a resolution previously shown to be adequate for reproducing the 2D cylinder wake dynamics [65].

Spatio-temporal simulations are performed in the range $Re \in [20, 60]$. The streamwise u and normal-to-flow v velocity components are stored with a time step $\Delta t = 0.2$, for a total computational time $T = 400$, yielding 2000 temporal realizations of the velocity field for each value of Re.

For relatively low Reynolds numbers ($Re = 20$ and $Re = 40$) the flow is steady, characterized by a recirculation wake region ($u < 0$) whose extent increases with Re (Fig. 2). As Re increases up to $Re = 60$, the velocity field exhibits periodic spatio-temporal oscillations due to the vortex-shedding phenomenon originating behind the cylinder. The onset of the periodic regime is determined by an instability developing in the recirculation wake region near $Re_{cr} \approx 49$, known to be the manifestation of an Andronov–Hopf bifurcation [64].

4. Results

4.1 POD basis identification

For the cylinder configuration, we employed the parameters $Re_{min} = 40$, $Re_{max} = 60$, $N_g = 7800$, $N_t = 1000$, $N_{Re} = 11$, for a total of $M = 22000$ snapshots used to build the POD basis of Section 2.2.

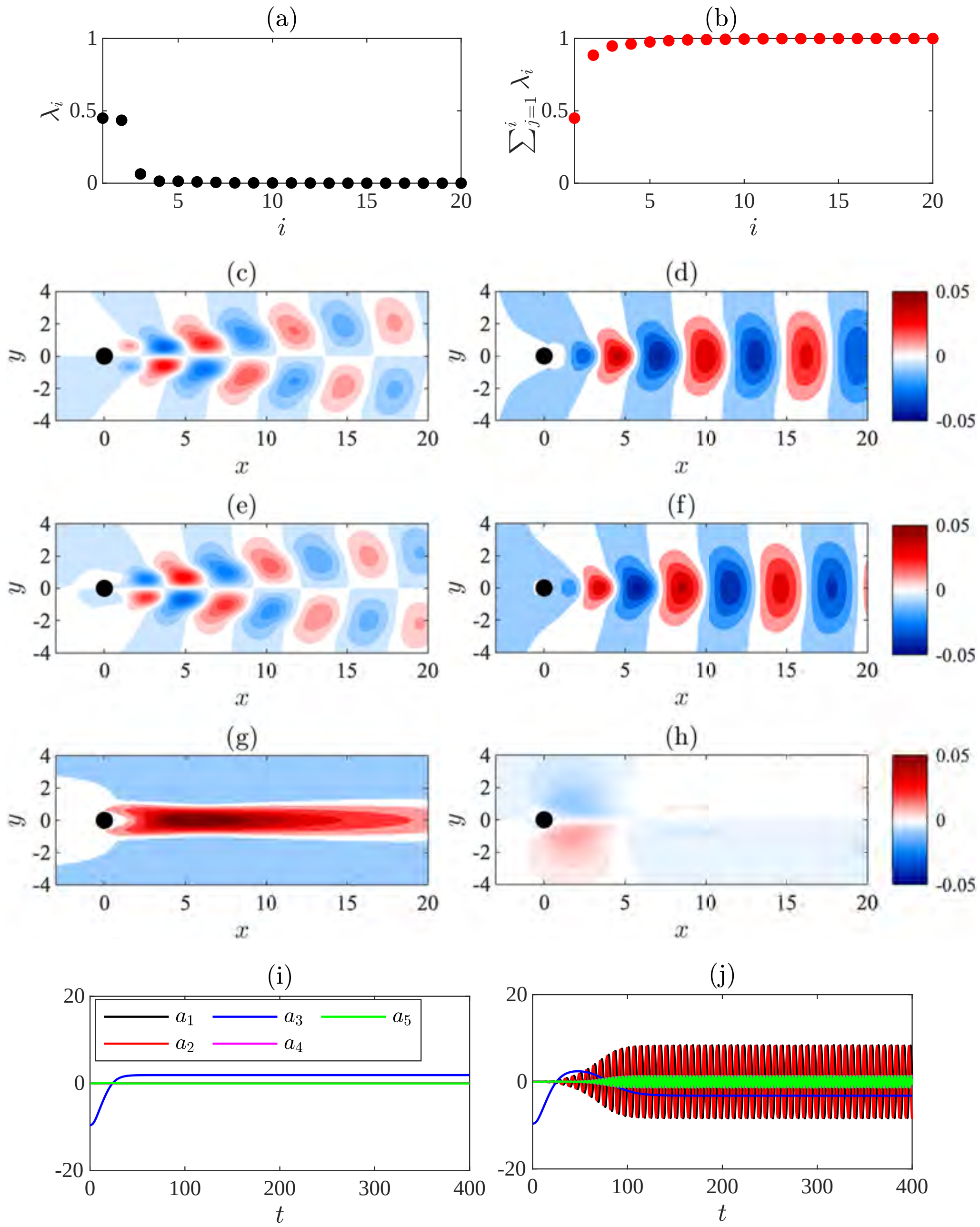

Figure 3: Eigenvalue spectrum and corresponding cumulative sum of the cylinder flow ((a)-(b)). Panels (c)-(d), (e)-(f) report the leading spatial modes $\boldsymbol{\varphi}_1$ and $\boldsymbol{\varphi}_2$ for u (left) and v (right) fields. Panels (g)-(h) show the temporal evolution of the velocity field projections a_i on the five leading modes for $Re = 40$ and $Re = 60$, respectively.

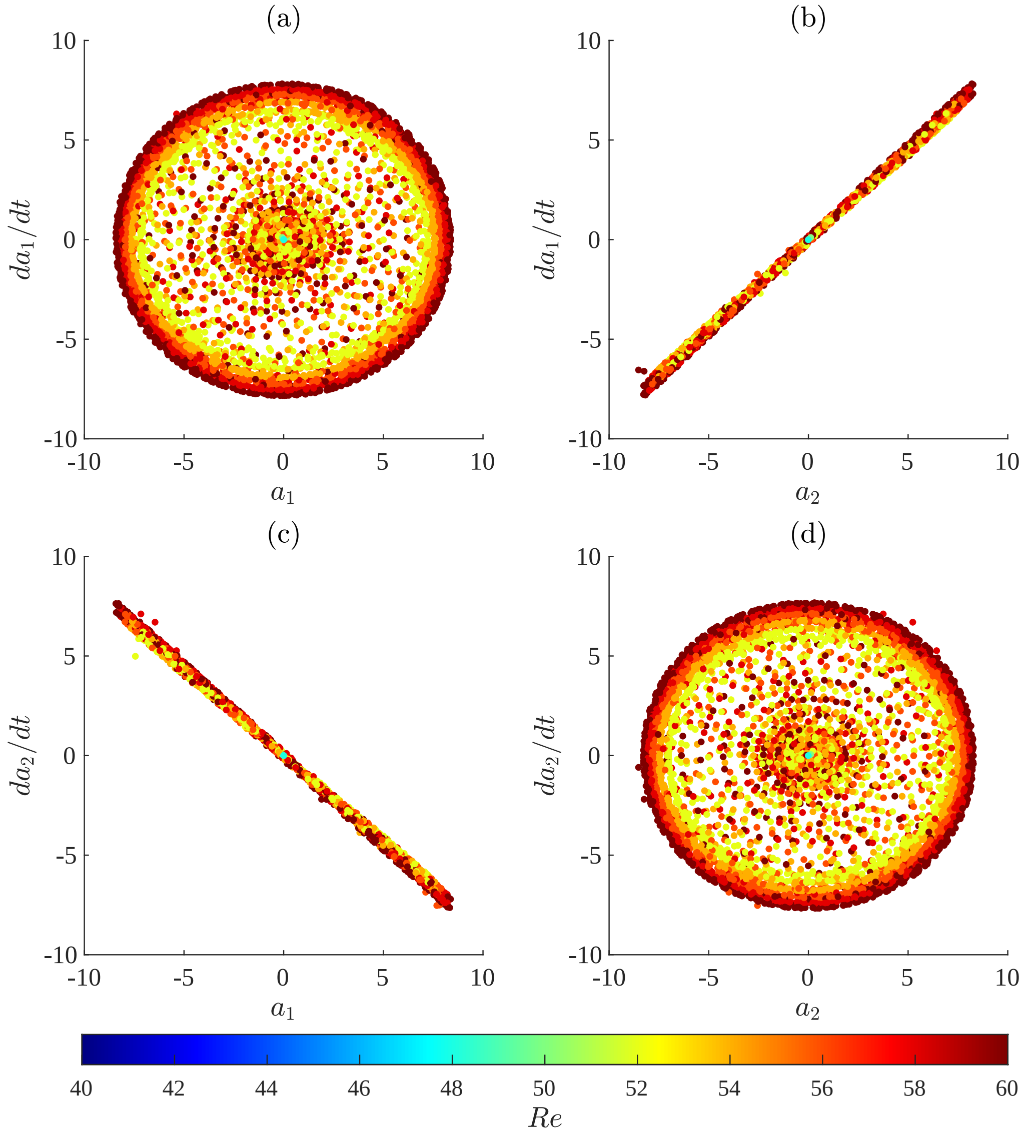

Figure 4: Numerical data set used to train the POD-GPR model of the circular cylinder flow latent dynamics in the (Re, a_1, a_2) space, colored by Reynolds number Re.

Figure 3(a)-(b) shows the POD eigenvalue spectrum and cumulative energy, while panels (c)-(f) show the leading spatial modes $\boldsymbol{\varphi}_1$ and $\boldsymbol{\varphi}_2$. These first two modes are physically associated with the periodic von Kármán street of vortices establishing downstream of the cylinder for $Re > Re_{cr}$ [72]. A third mode, associated with a shift-mode characteristic of the transient dynamics from the onset of vortex shedding to the periodic wake, does not contribute additional information relevant to the bifurcation itself, while the fourth and fifth modes (not shown) represent higher harmonics of the leading two. By inspecting the temporal evolution of the velocity field projections $a_i(t)$ for $Re = 40$ and $Re = 60$ (Fig. 3(g)-(h)), it is clear that $\boldsymbol{\varphi}_1$ and $\boldsymbol{\varphi}_2$ represent the minimal number of modes required to describe the bifurcation separating the steady and periodic flow regimes. We therefore retain the leading $d = 2$ modes to train the surrogate GPR model. Importantly, in this case POD automatically identifies the minimal dimensionality needed to capture the bifurcation—as we discuss in Section 5, this is a consequence of the Andronov–Hopf bifurcation being a *primary* instability, and it no longer holds for more complex, secondary bifurcation scenarios.

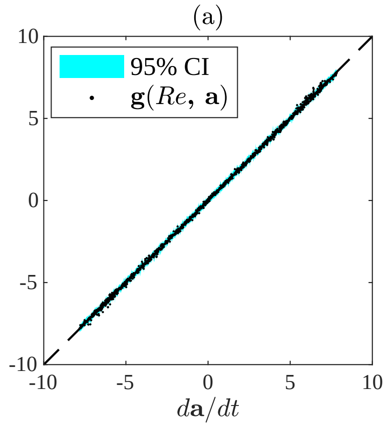

Figure 5: Uncertainty quantification of the GPR reduced-order model on the testing data set for the cylinder flow configuration. For given input data, the model predictions of $d\mathbf{a}/dt$ are shown both in terms of expected (mean) values (black dots) and 95% confidence intervals (cyan band). The black dashed line denotes the quadrant bisector.

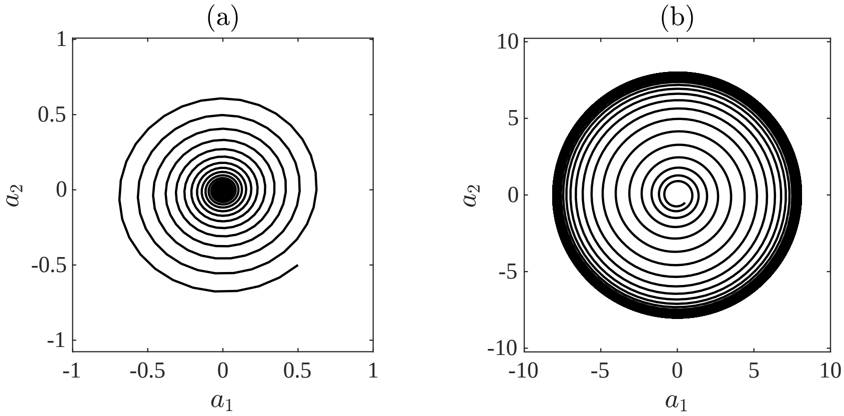

Figure 6: Reduced-order dynamics of the cylinder flow as predicted by time integration of the POD-GPR model: $Re = 45$ (a); $Re = 55$ (b).

4.2 ROM training and predictive uncertainty

The available data set was randomly partitioned into training (60%) and testing (40%) subsets, and used to identify the reduced dynamical operator of Eq. (14), with the time derivatives $d\mathbf{a}/dt$ approximated using finite differences with a time step $\Delta t = 0.2$. The geometry of the resulting training data in the (Re, a_1, a_2) latent space (Fig. 4) is a smooth, low-curvature two-dimensional manifold parametrized by the Reynolds number and the leading modal amplitudes, consistent with the presence of a single primary instability. This structural simplicity facilitates the learning of an accurate reduced evolution operator directly in the POD linear subspace.

The predictive accuracy and associated uncertainty of the learned GPR model are illustrated in Fig. 5: for given inputs (Re, a_1, a_2), the GPR model predicts both the expected value of the reduced operator and its standard deviation, from which the 95% confidence intervals are computed. On the testing data set, the maximum standard deviation was found to be 2.03% of the corresponding mean value, confirming that the learned surrogate provides an accurate and robust approximation of the latent Navier–Stokes dynamics across the explored Reynolds number range.

The numerical integration of the POD-GPR reduced-order model is first assessed for two representative values of the Reynolds number, spanning both the steady laminar ($Re < Re_{cr}$) and periodic vortex-shedding ($Re > Re_{cr}$) regimes. Results are shown in Fig. 6, where the time evolution of the reduced

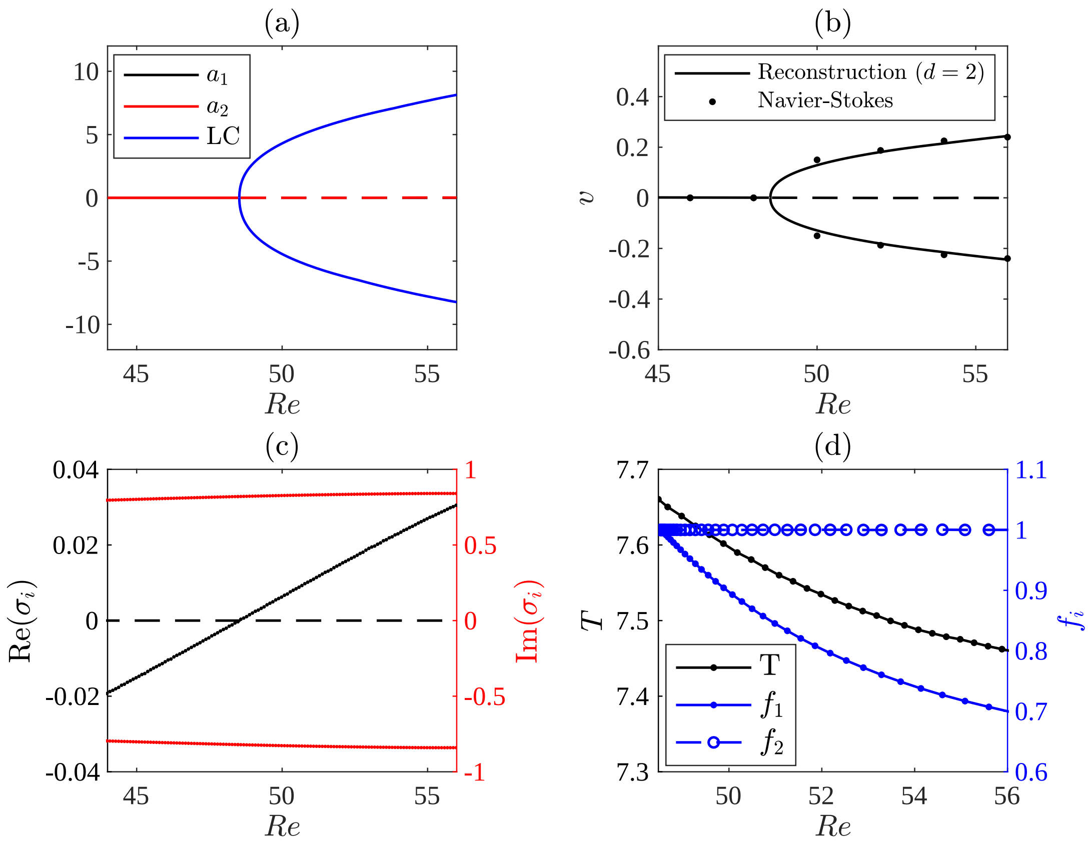

Figure 7: Numerical bifurcation diagram of the POD-based ROM of the cylinder flow by increasing the Reynolds number Re (a). A supercritical Hopf bifurcation occurs at $Re_{cr} = 48.48$: the stable fixed-point solution ($a_1 = a_2 = 0$) becomes unstable, giving rise to a branch of limit cycles LC (blue curve). In panel (b), the high-dimensional bifurcation diagram (black continuous curve) is reconstructed in terms of the v velocity component at $x = 10$, $y = 0$; values from the Navier–Stokes solutions are also reported for comparison (black dots). Panel (c): a complex-conjugate pair of eigenvalues (red circles) become unstable (i.e., $\mathrm{Re}(\sigma_i) > 0$ for $i = 1, 2$) for $Re > Re_{cr}$. Panel (d): limit-cycle period T (black curve) and Floquet multipliers f_1 and f_2 (blue curves) as a function of Re, obtained from limit-cycle branch continuation.

coordinates a_1 and a_2 in phase space is reported for $Re = 45$ (panel (a)) and $Re = 55$ (panel (b)), using initial conditions from the (unseen) test data set. The learned surrogate model qualitatively reproduces the cylinder wake dynamics in both regimes: the reduced coordinates asymptotically converge to the fixed-point stable solution $a_1 = a_2 = 0$ for $Re = 45$, while periodic limit-cycle oscillations are recovered for $Re = 55$.

4.3 Andronov–Hopf bifurcation and stability analysis

Once the predictive capability of the POD-based ROM has been validated, a numerical bifurcation diagram is constructed using the continuation method of Section 2.5. The results, presented in Fig. 7, clearly identify the onset of a Hopf bifurcation at the critical Reynolds number $Re_{cr} = 48.48$, in excellent agreement with the reference value $Re_{cr} \approx 49$ reported for the full Navier–Stokes system [64].

For $Re < Re_{cr}$, the system exhibits a single stable fixed-point attractor, $a_1 = a_2 = 0$ (overlapping solid black and red curves in Fig. 7(a)). As Re increases beyond Re_{cr}, this fixed point becomes unstable (dashed curves), and a branch of stable limit cycles (LC) emerges (blue curve). Figure 7(c) shows the eigenvalues of the Jacobian matrix of the learned system (14) as a function of Re: as is characteristic of a Hopf bifurcation, a complex-conjugate pair of eigenvalues crosses the imaginary axis and becomes

Quantity	Value
Latent dimension d	2
Critical Reynolds number Re_{cr} (POD-GPR ROM)	48.48
Reference Re_{cr} from the literature [64]	≈ 49
Floquet multiplier f_1 at Re_{cr}	1 (decreasing for $Re > Re_{cr}$)
Floquet multiplier f_2 (neutral direction)	1 (constant)
Maximum GPR standard deviation on test set	2.03%
Maximum relative error, lifted vs. DNS solution	12% (at $Re = 50$)

Table 1: Summary of the key quantities computed for the Andronov–Hopf bifurcation of the cylinder wake flow with the POD-GPR ROM.

unstable ($\text{Re}(\sigma_i) > 0$ for $i = 1, 2$) for $Re > Re_{cr}$, with the imaginary part—corresponding to the oscillation frequency of the resulting limit cycles—increasing slightly with Re, consistent with previous findings [65].

The continuation along the limit-cycle branch further enables the computation of the oscillation period T and the associated Floquet multipliers f_1 and f_2 (Fig. 7(d)), which characterize the stability of the periodic solutions. The first Floquet multiplier f_1 equals one at the bifurcation point and decreases monotonically with increasing Re, reflecting the increasing stability of the limit cycle as the Reynolds number grows. The second multiplier f_2 remains constant and equal to 1 throughout the branch, an expected trivial result corresponding to the neutral direction associated with the time invariance of the periodic orbit. The values $f_1 = f_2 = 1$ at the bifurcation point are consistent with the theoretical prediction for a supercritical Hopf bifurcation. Table 1 summarizes the key quantities computed along the branch.

Finally, by addressing the pre-image problem via the closed-form POD lifting map of Eq. (6), the POD-GPR reduced-order solutions are reconstructed back to the original high-dimensional physical space, yielding the full bifurcation diagram of Fig. 7(b). For comparison, we also report the Navier–Stokes solutions (black dots) in terms of the transverse velocity v stored at $x = 10$, $y = 0$; for $Re > Re_{cr}$, both the maximum and minimum amplitude of the v oscillations are considered. The high-dimensional bifurcation diagram is accurately reconstructed by the minimal $d = 2$ ROM across the whole Reynolds number range considered, with a maximum relative percentage error of 12% at $Re = 50$.

5. Discussion: towards more complex bifurcation scenarios

The results of Section 4 show that a genuinely PDE-free pipeline—POD restriction, GPR-based latent-dynamics learning, and MATCONT continuation—is sufficient to reconstruct, with high accuracy, the full Andronov–Hopf bifurcation diagram of the cylinder wake flow, including the stability of the emerging limit cycles and their Floquet multipliers. This success hinges on a structural property of the problem: the Hopf bifurcation of the cylinder wake is a *primary* instability, and the corresponding latent manifold is smooth and of low curvature, so that a linear embedding such as POD automatically identifies the correct minimal dimension ($d = 2$) of the underlying normal-form dynamics.

This is, however, not guaranteed in general. When a flow undergoes a *secondary* bifurcation—e.g., a Neimark–Sacker bifurcation destabilizing an already-established limit cycle and giving rise to quasi-periodic dynamics on an invariant torus—or a symmetry-breaking pitchfork bifurcation, the geometry of the latent manifold becomes considerably more intricate, exhibiting curvature, twisting, and folding that reflect the coexistence and interaction of multiple time scales. In such cases, POD may fail to identify the correct intrinsic dimensionality of the data, or may require additional modes that do not correspond to the true, parsimonious normal-form dimension, thereby losing dynamical-systems and numerical-analysis insight, and, in the worst case, becoming unable to reproduce the correct bifurcation structure altogether. Nonlinear manifold-learning techniques, such as parsimonious Diffusion Maps [42, 45], are then required to correctly uncover the intrinsic dimension and provide a geometrically consistent latent parametrization of the flow—at the cost of an inherently ill-posed pre-image problem, which must be addressed with dedicated techniques such as the k-nearest-neighbour algorithm [73, 44] in place of the closed-form POD lifting map of Eq. (6).

This more demanding regime is thoroughly investigated in a companion study [1], where the same restrict–learn–lift pipeline presented here, extended with a Diffusion-Maps-based restriction stage, is applied to two additional benchmark configurations: the planar sudden-expansion (Coanda) channel flow, which undergoes a symmetry-breaking pitchfork bifurcation as Re increases, and the fluidic pinball, which exhibits a secondary Neimark–Sacker bifurcation leading to the birth of an invariant torus. There, it is shown that Diffusion-Maps-based ROMs correctly identify the minimal latent dimension in both cases—including the five-dimensional parsimonious embedding required to capture the Neimark–Sacker bifurcation of the fluidic pinball—and enable, to the best of our knowledge for the first time, the continuation and Floquet stability analysis of the resulting quasi-periodic solutions directly within a state-of-the-art bifurcation toolkit such as MATCONT, whereas POD-based ROMs of the same dimension are shown to fail in reliably reproducing this behaviour.

6. Conclusions

We have presented a PDE-free, data-driven "restrict–learn–lift" framework that combines Proper Orthogonal Decomposition, Gaussian Process regression, and the numerical bifurcation-analysis toolkit MATCONT to perform numerical bifurcation and stability analysis of high-fidelity Navier–Stokes simulations without ever requiring the assembly or factorization of the full-order Jacobian. On the benchmark wake flow past a circular cylinder, the resulting minimal, two-dimensional POD-GPR ROM accurately reconstructs the Andronov–Hopf bifurcation diagram, including the continuation of stable and unstable branches, the period of the emerging limit cycles, and their Floquet multipliers, with a maximum relative error of 12% with respect to the full-order Navier–Stokes solutions and a maximum GPR predictive uncertainty of 2.03%.

The cylinder wake case illustrates a favourable, and comparatively simple, scenario in which a linear manifold-learning technique such as POD is sufficient to identify the correct minimal dimension of the latent dynamics. As discussed in Section 5, and as thoroughly demonstrated in a companion study [1], this is generally no longer the case for more demanding, secondary bifurcation scenarios—such as symmetry-breaking pitchfork bifurcations or Neimark–Sacker bifurcations leading to quasi-periodic, torus-like dynamics—for which nonlinear manifold-learning techniques, such as parsimonious Diffusion Maps, are required to correctly capture the intrinsic dimensionality and geometry of the underlying normal-form dynamics. Future work will focus on extending the present PDE-free framework to codimension-two and global bifurcations, which underlie the onset of turbulence, and on the identification of low-dimensional attracting manifolds and the corresponding normal forms for such global bifurcations.

Acknowledgements

A.D.P. acknowledges the CINECA award under the ISCRA initiative, for the availability of high-performance computing resources and support. C.S. acknowledges partial support from the PNRR MUR, projects PE0000013-Future Artificial Intelligence Research-FAIR & CN0000013 CN HPC - National Centre for HPC, Big Data and Quantum Computing, Gruppo Nazionale Calcolo Scientifico-Istituto Nazionale di Alta Matematica (GNCS-INdAM).

References

[1] A. Della Pia, D. G. Patsatzis, G. Rozza, L. Russo, and C. Siettos. Surrogate normal-forms for the numerical bifurcation and stability analysis of navier-stokes flows via machine learning.

Communications in Nonlinear Science and Numerical Simulation, 2026. In press. Available at `https://www.sciencedirect.com/science/article/pii/S100757042600496X`.

[2] E. J. Doedel. Auto: A program for the automatic bifurcation analysis of autonomous systems. *Congr. Numer*, 30(265-284):25–93, 1981.

[3] A. Dhooge, W. Govaerts, and Yu. A. Kuznetsov. Matcont: a matlab package for numerical bifurcation analysis of odes. *ACM Trans. Math. Software*, 29:141–164, 2003.

[4] W. Govaerts, Y. A Kuznetsov, and A. Dhooge. Numerical continuation of bifurcations of limit cycles in matlab. *SIAM journal on scientific computing*, 27(1):231–252, 2005.

[5] M. E. Kavousanakis, L. Russo, C. I. Siettos, A. G. Boudouvis, and G. C. Georgiou. A timestepper approach for the systematic bifurcation and stability analysis of polymer extrusion dynamics. *Journal of non-newtonian fluid mechanics*, 151(1-3):59–68, 2008.

[6] J. Sánchez, M. Net, B. Garcıa-Archilla, and C. Simó. Newton–krylov continuation of periodic orbits for navier–stokes flows. *Journal of Computational Physics*, 201(1):13–33, 2004.

[7] G. Samaey, W. Vanroose, D. Roose, and I. G. Kevrekidis. Newton–krylov solvers for the equation-free computation of coarse traveling waves. *Computer Methods in Applied Mechanics and Engineering*, 197(43-44):3480–3491, 2008.

[8] J. Sanchez, F. Marques, and J. M. Lopez. A continuation and bifurcation technique for navier–stokes flows. *Journal of Computational Physics*, 180(1):78–98, 2002.

[9] J. Sánchez and M. Net. On the multiple shooting continuation of periodic orbits by newton–krylov methods. *International Journal of Bifurcation and Chaos*, 20(01):43–61, 2010.

[10] M. Net and J. Sánchez. Continuation of bifurcations of periodic orbits for large-scale systems. *SIAM Journal on Applied Dynamical Systems*, 14(2):674–698, 2015.

[11] I. Waugh, S. Illingworth, and M. Juniper. Matrix-free continuation of limit cycles for bifurcation analysis of large thermoacoustic systems. *Journal of Computational Physics*, 240:225–247, 2013.

[12] G. Haller. Modeling nonlinear dynamics from equations and data with applications to solids, fluids, and controls, 2025.

[13] R. Temam. *Navier–Stokes equations and nonlinear functional analysis*. SIAM, 1995.

[14] E. S. Titi. On approximate inertial manifolds to the navier-stokes equations. *Journal of mathematical analysis and applications*, 149(2):540–557, 1990.

[15] A. Quarteroni and G. Rozza. Numerical solution of parametrized navier–stokes equations by reduced basis methods. *Numerical methods for partial differential equations: an international journal*, 23(4):923–948, 2007.

[16] A. Quarteroni and G. Rozza. *Reduced order methods for modeling and computational reduction*, volume 9. Springer, 2014.

[17] R. Vinuesa and S. L. Brunton. Enhancing computational fluid dynamics with machine learning. *Nature Computational Science*, 2:358–366, 2022.

[18] S. Hijazi, G. Stabile, A. Mola, and G. Rozza. Data-driven pod-galerkin reduced order model for turbulent flows. *Journal of Computational Physics*, 416:109513, 2020.

[19] F. Pichi, F. Ballarin, G. Rozza, and J. S. Hesthaven. An artificial neural network approach to bifurcating phenomena in computational fluid dynamics. *Comput. Fluids*, 254:105813, 2023.

[20] R. Seydel. *Practical bifurcation and stability analysis*, volume 5. Springer Science & Business Media, 2009.

[21] M. W. Hirsch, C. C. Pugh, and M. Shub. Invariant manifolds. *Bulletin of the American Mathematical Society*, 76(5):1015–1019, 1970.

[22] T. Gallay and C. E. Wayne. Invariant manifolds and the long-time asymptotics of the navier-stokes and vorticity equations on r2. *Archive for Rational Mechanics and Analysis*, 163:209–258, 2002.

[23] C. Siettos. Equation-free computation of coarse-grained center manifolds of microscopic simulators. *Journal of Computational Dynamics*, 1(2):377–389, 2014.

[24] S. Wiggins. *Normally hyperbolic invariant manifolds in dynamical systems*, volume 105. Springer Science & Business Media, 2013.

[25] C. Siettos and L. Russo. A numerical method for the approximation of stable and unstable manifolds

of microscopic simulators. *Numerical Algorithms*, 89(3):1335–1368, 2022.

[26] G. Haller and S. Ponsioen. Nonlinear normal modes and spectral submanifolds: existence, uniqueness and use in model reduction. *Nonlinear dynamics*, 86:1493–1534, 2016.

[27] T. Breunung and G. Haller. Explicit backbone curves from spectral submanifolds of forced-damped nonlinear mechanical systems. *Proceedings of the Royal Society A: Mathematical, Physical and Engineering Sciences*, 474(2213):20180083, 2018.

[28] G. Buza. Spectral submanifolds of the navier–stokes equations. *SIAM Journal on Applied Dynamical Systems*, 23(2):1052–1089, 2024.

[29] C. Foias, G. R. Sell, and R. Temam. Inertial manifolds for nonlinear evolutionary equations. *Journal of differential equations*, 73(2):309–353, 1988.

[30] P. Constantin, C. Foias, B. Nicolaenko, and R. Témam. Spectral barriers and inertial manifolds for dissipative partial differential equations. *Journal of Dynamics and Differential Equations*, 1:45–73, 1989.

[31] P. Constantin, C. Foias, B. Nicolaenko, and R. Temam. *Integral manifolds and inertial manifolds for dissipative partial differential equations*, volume 70. Springer Science & Business Media, 2012.

[32] G. Stabile and G. Rozza. Finite volume pod-galerkin stabilised reduced order methods for the parametrised incompressible navier–stokes equations. *Computers & Fluids*, 173:273–284, 2018.

[33] J. S. Hesthaven and S. Ubbiali. Non-intrusive reduced order modelling of nonlinear problems using neural networks. *Journal of Computational Physics*, 363:55–78, 2018.

[34] M. Girfoglio, A. Quaini, and G. Rozza. A pod-galerkin reduced order model for the navier–stokes equations in stream function-vorticity formulation. *Computers & Fluids*, 244:105536, 2022.

[35] A. E. Deane, I. G. Kevrekidis, G. E. Karniadakis, and S. A. Orszag. Low-dimensional models for complex geometry flows: Application to grooved channels and circular cylinders. *Physics of Fluids A: Fluid Dynamics*, 3(10):2337–2354, 1991.

[36] X. Ma and G. E. Karniadakis. A low-dimensional model for simulating three-dimensional cylinder flow. *Journal of Fluid Mechanics*, 458:181–190, 2002.

[37] C. W. Rowley. Model reduction for fluids, using balanced proper orthogonal decomposition. *International Journal of Bifurcation and Chaos*, 15(03):997–1013, 2005.

[38] S. L. Brunton, B. R. Noack, and P. Koumoutsakos. Machine learning for fluid mechanics. *Annual review of fluid mechanics*, 52(1):477–508, 2020.

[39] R. R. Coifman, S. Lafon, A. B. Lee, M. Maggioni, B. Nadler, F. Warner, and S. W. Zucker. Geometric diffusions as a tool for harmonic analysis and structure definition of data: diffusion maps. *Proc. Natl. Acad. Sci.*, 102(21):7426–7431, 2005.

[40] R. R. Coifman and S. Lafon. Geometric harmonics: a novel tool for multiscale out-of-sample extension of empirical functions. *Appl. Comput. Harmon. Anal.*, 21(1):31–52, 2006.

[41] B. Nadler, S. Lafon, R. R. Coifman, and I. G. Kevrekidis. Diffusion maps, spectral clustering and reaction coordinates of dynamical systems. *Applied and Computational Harmonic Analysis*, 21(1):113–127, 2006.

[42] C. J. Dsilva, R. Talmon, R. R. Coifman, and I. G. Kevrekidis. Parsimonious representation of nonlinear dynamical systems through manifold learning: a chemotaxis case study. *Appl. Comput. Harmon. Anal.*, 44(3):759–773, 2018.

[43] E. Galaris, G. Fabiani, I. Gallos, I. Kevrekidis, and C. Siettos. Numerical bifurcation analysis of pdes from lattice boltzmann model simulations: a parsimonious machine learning approach. *Journal of Scientific Computing*, 92(34):1–30, 2022.

[44] D. Patsatzis, L. Russo, I. G. Kevrekidis, and C. Siettos. Data-driven control of agent-based models: An equation/variable-free machine learning approach. *Journal of Computational Physics*, 478(111953), 2023.

[45] A. Della Pia, D. G. Patsatzis, L. Russo, and C. Siettos. Learning the latent dynamics of fluid flows from high-fidelity numerical simulations using parsimonious diffusion maps. *Physics of Fluids*, 36(105187):1–19, 2024.

[46] S. L. Brunton, J. L. Proctor, and J. N. Kutz. Discovering governing equations from data by sparse

identification of nonlinear dynamical systems. *Proceedings of the National Academy of Sciences*, 113(15):3932–3937, 2016.

[47] K. Champion, B. Lusch, J. N. Kutz, and S. L. Brunton. Data-driven discovery of coordinates and governing equations. *Proceedings of the National Academy of Sciences*, 116(45):22445–22451, 2019.

[48] P. Conti, G. Gobat, S. Fresca, A. Manzoni, and A. Frangi. Reduced order modeling of parametrized systems through autoencoders and sindy approach: continuation of periodic solutions. *Computer Methods in Applied Mechanics and Engineering*, 411:116072, 2023.

[49] S. Lee, M. Kooshkbaghi, K. Spiliotis, C. I. Siettos, and I. G. Kevrekidis. Coarse-scale pdes from fine-scale observations via machine learning. *Chaos: An Interdisciplinary Journal of Nonlinear Science*, 30(1):013141, 2020.

[50] G. Fabiani, N. Evangelou, T. Cui, J. M. Bello-Rivas, C. P. Martin-Linares, C. Siettos, and I. G. Kevrekidis. Task-oriented machine learning surrogates for tipping points of agent-based models. *Nature communications*, 15(1):4117, 2024.

[51] Z. Y. Wan and T. P. Sapsis. Reduced-space gaussian process regression for data-driven probabilistic forecast of chaotic dynamical systems. *Physica D: Nonlinear Phenomena*, 345:40–55, 2017.

[52] D. Stephenson, J. R. Kermode, and D. A. Lockerby. Accelerating multiscale modelling of fluids with on-the-fly gaussian process regression. *Microfluidics and Nanofluidics*, 22(12):139, 2018.

[53] Z. Ma and W. Pan. Data-driven nonintrusive reduced order modeling for dynamical systems with moving boundaries using gaussian process regression. *Computer Methods in Applied Mechanics and Engineering*, 373:113495, 2021.

[54] G. Ortali, N. Demo, and G. Rozza. A gaussian process regression approach within a data-driven pod framework for engineering problems in fluid dynamics. *Mathematics in Engineering*, 4(3):1–16, 2022.

[55] M. Hess, A. Alla, A. Quaini, G. Rozza, and M. Gunzburger. A localized reduced-order modeling approach for pdes with bifurcating solutions. *Computer Methods in Applied Mechanics and Engineering*, 351:379–403, 2019.

[56] M. Pintore, F. Pichi, M. Hess, G. Rozza, and C. Canuto. Efficient computation of bifurcation diagrams with a deflated approach to reduced basis spectral element method. *Advances in Computational Mathematics*, 47:1–39, 2021.

[57] F. Pichi, M. Strazzullo, F. Ballarin, and G. Rozza. Driving bifurcating parametrized nonlinear pdes by optimal control strategies: application to navier–stokes equations with model order reduction. *ESAIM: Mathematical Modelling and Numerical Analysis*, 56(4):1361–1400, 2022.

[58] M. Khamlich, F. Pichi, and G. Rozza. Model order reduction for bifurcating phenomena in fluid-structure interaction problems. *International Journal for Numerical Methods in Fluids*, 94(10):1611–1640, 2022.

[59] I. G. Kevrekidis, C. W. Gear, J. M. Hyman, P. G. Kevrekidis, O. Runborg, and C. Theodoropoulos. Equation-free, coarse-grained multiscale computation: Enabling microscopic simulators to perform system-level analysis. *Communications in Mathematical Sciences*, 1(4):715–762, 2003.

[60] L. Russo, C. I. Siettos, and I. G. Kevrekidis. Reduced computations for nematic-liquid crystals: A timestepper approach for systems with continuous symmetries. *Journal of Non-Newtonian Fluid Mechanics*, 146(1):51–58, 2007.

[61] A. Dhooge, W. Govaerts, Y. A. Kuznetsov, W. Mestrom, A. M. Riet, and B. Sautois. Matcont and cl matcont: Continuation toolboxes in matlab. *Universiteit Gent, Belgium and Utrecht University, The Netherlands*, 2006.

[62] J. Sierra, D. Fabre, V. Citro, and F. Giannetti. Bifurcation scenario in the two-dimensional laminar flow past a rotating cylinder. *Journal of Fluid Mechanics*, 905:A2, 2020.

[63] S. Sirisup, G. E. Karniadakis, D. Xiu, and I. G. Kevrekidis. Equation-free/galerkin-free pod-assisted computation of incompressible flows. *Journal of Computational Physics*, 207(2):568–587, 2005.

[64] C. H. K. Williamson. Vortex dynamics in the cylinder wake. *Annual Review of Fluid Mechanics*, 28:477–539, 1996.

[65] F. Giannetti and P. Luchini. Structural sensitivity of the first instability of the cylinder wake. *Journal of Fluid Mechanics*, 581:167–197, 2007.

[66] J. L. Lumley. The structure of inhomogeneous turbulent flows. *Proceedings of the International Colloquium on the Fine Scale Structure of the Atmosphere and Its Influence on Radio Wave Propagation*, edited by A. M. Yaglam, and V. I. Tatarsky, Doklady Akademii Nauk SSSR, Nauka, Moscow, 1967.

[67] L. Sirovich. Turbulence and the dynamics of coherent structures, parts i–iii. *Quarterly of Applied Mathematics*, 45(3):561–571, 1987.

[68] E. Chiavazzo, C. W. Gear, C. J. Dsilva, N. Rabin, and I. G. Kevrekidis. Reduced models in chemical kinetics via nonlinear data-mining. *Processes*, 2(1):112–140, 2014.

[69] P. G. Papaioannou, R. Talmon, I. G. Kevrekidis, and C. Siettos. Time-series forecasting using manifold learning, radial basis function interpolation, and geometric harmonics. *Chaos*, 32(8):083113, 2022.

[70] S. Popinet. Gerris: a tree-based adaptive solver for the incompressible Euler equations in complex geometries. *Journal of Computational Physics*, 190(2):572–600, 2003.

[71] Y. A. Kuznetsov, I. A. Kuznetsov, and Y. Kuznetsov. *Elements of applied bifurcation theory*, volume 112. Springer, 1998.

[72] B. R. Noack, K. Afanasiev, M. Morzyński, G. Tadmor, and F. Thiele. A hierarchy of low-dimensional models for the transient and post-transient cylinder wake. *Journal of Fluid Mechanics*, 497:335–363, 2003.

[73] Tracy Chin, Jacob Ruth, Clayton Sanford, Rebecca Santorella, Paul Carter, and Björn Sandstede. Enabling equation-free modeling via diffusion maps. *Journal of Dynamics and Differential Equations*, 36(Suppl 1):415–434, 2024.